Supporting Information

Defect Assisted Protein HP35 Denaturation on Graphene

Zonglin Gu[1,‡], Wei Song[2,‡], Serena H. Chen[3], Baoyu Li[1], Weifeng Li[4], and Ruhong Zhou[1,3,5,*]

1. State Key Laboratory of Radiation Medicine and Protection, School for Radiological and Interdisciplinary Sciences (RAD-X), and Collaborative Innovation Center of Radiation Medicine of Jiangsu Higher Education Institutions, Soochow University, Suzhou 215123, China
2. Institute of Quantitative Biology, Department of Physics, Zhejiang University, Hangzhou 310027, China
3. IBM Thomas J. Watson Research Center, Yorktown Heights, NY 10598, USA
4. School of Physics, Shandong University, Jinan 250100, China
5. Department of Chemistry, Columbia University, New York, NY 10027, USA

*Corresponding author, E-mail: ruhongz@us.ibm.com

1. Simulation Details

We chose HP35 because its folding and unfolding dynamics have been extensively studied, which features general properties associated with common globular proteins despite its small size.[1-4] The initial protein structure was obtained from the Protein Data Bank. The PDB ID is 1YRF.[5] Additionally, YAP65 WW domain (PDB ID 1JMQ[6]), constructed by three β-sheet segments, was also used to investigate its unfolding capacity on D-Gra. The simulation box includes HP35/YAP65, graphene, water, and counter ions. The box contents can be found in Table S1.

The simulations were carried out with the GROMACS (version 4.6.6) software package[7] using the CHARMM27 force field.[8-9] Following previous work of Seminario and coworkers,[10] the CHARMM CA atom type was assigned to the C atoms of I-Gra and the C atoms at the defect-free regions of D-Gra. For defects, we adopted the topology of Asp sidechain in CHARMM to mimic the carboxyl groups at the defect edges. Six atom types from CHARMM were adopted for the D-Gra model, for which the Lennard-Jones parameters and atom charges can be found in Table S2. We adopted the TIP3P model[11] for water molecules.

All simulations were conducted at constant temperature of 300 K using v-rescale thermostat.[12] Semi-isotropic pressure coupling along the *z* direction was used to maintain constant pressure of 1 atm, using Parrinello-Rahman barostat.[13] Periodic boundary conditions were applied in all directions. In fact, graphene flakes usually exhibit significant wrinkle on its surface,[14] especially when defected. However, researchers commonly fixed or restrained 2-dimensional (2D) nanomaterials to explore the interaction between 2D nanomaterials and various biomolecules using molecular dynamics simulation approach.[15-20] Also, this method was applied to probe the theoretical nanotoxicity.[21-22] Therefore, following the similar pathway, the sp^2 C atoms of D-Gra and I-Gra were restrained at their initial positions. The long-range electrostatic interactions were treated with the PME method,[23-24] and the van der Waals (vdW) interactions were calculated with a cutoff distance of 10 Å. All bonds were maintained constant at their equilibrium values with the LINCS algorithm,[25] and water geometry was constrained using the SETTLE algorithm.[26] Each system was first energy-

minimized with the steepest descent algorithm, followed by 20 ns of pre-equilibration with position restraints applied to the protein. Random initial velocities were then assigned to HP35 and solvent atoms. Three independent trajectories of 500 ns were conducted for each system. A time step of 2.0 fs was used, and data were collected every 1 ps. The VMD software[27] was used to analyze and visualize the simulation results.

Table S1. Simulation box contents of the five systems.

	HP35/D-Gra	HP35/I-Gra	HP35/D-Gra in 0.15 M NaCl	HP35/D-Gra in 0.15 M $MgCl_2$	YAP65/D-Gra
box size (nm^3)	12.48×12.72×7.00	12.48×12.72×7.05	12.48×12.72×7.0	12.48×12.72×6.9	12.48×12.72×6.9
number of water molecules	34,122	34,338	33,922	33,972	33,965
ion	52 Na^+	2 Cl^-	100 Na^+, 48 Cl^-	100 Mg^{2+}, 148 Cl^-	100 Na^+, 47 Cl^-
total number of atoms	109,120	109,718	108,720	108,820	108,811

Table S2. The force field parameters. The positions of the atoms (index in the brackets) can be found in the figure below.

	Atom type	ε (kcal/mol)	σ (nm)	charge
C (1)	**CA**	0.070	0.3550	0.0
C (2)	**CA**	0.070	0.3550	-0.1150
H (3)	**HA**	0.022	0.2352	0.1150
C (4)	**CA**	0.070	0.3550	-0.1966
C (5)	**CC**	0.070	0.3564	0.7994
O (6)	**OC**	0.120	0.3029	-0.8014

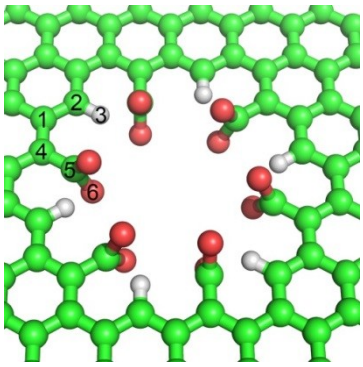

2. Distribution of the defects on D-Gra.

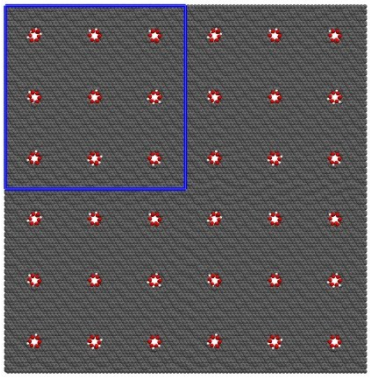

Figure S1. The defects are distributed roughly evenly on the graphene surface as a simple model for illustration, with a distance of about 3.2 nm between any two neighboring defects. The periodic images in the xy-plane are shown for clarity. The blue square indicates the box size. Red and gray spheres represent oxygen and carbon atoms, respectively.

3. The conformations of aromatic residues before and after binding onto D-Gra/I-Gra surfaces.

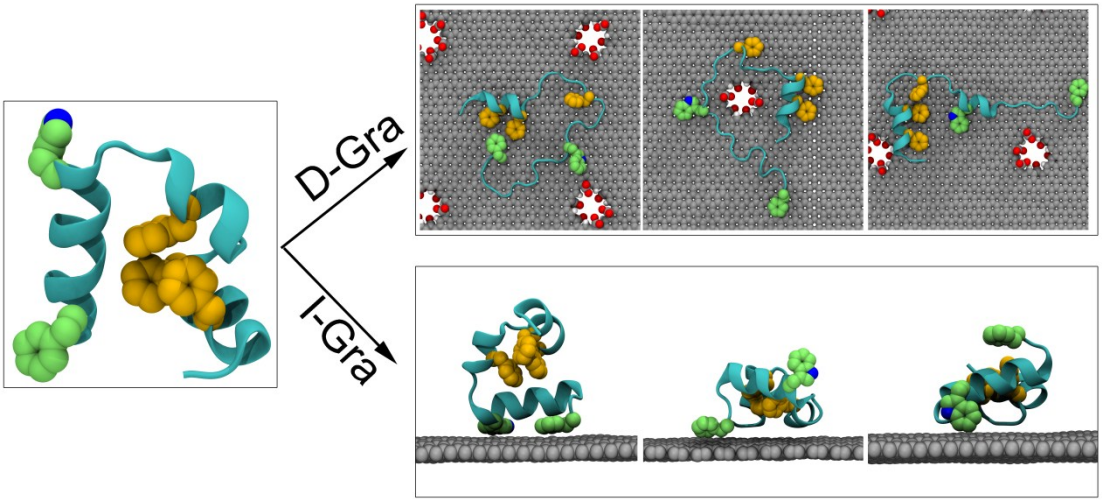

Figure S2. The conformations of aromatic residues before and after binding onto D-Gra/I-Gra surfaces. HP35 is shown in ribbon representation. The carbon atoms of D-Gra/I-Gra are in gray, oxygen in red, and hydrogen in white. The aromatic residues exposed to solvent are shown with lime (carbon) and blue (nitrogen) spheres while the aromatic residues buried in the hydrophobic core are shown with orange spheres.

By comparing the five aromatic residues after binding the D-Gra/I-Gra surfaces (**Fig. S2**), we observed that, all aromatic residues lied on the D-Gra surface, and three of the five aromatic residues which form the inner hydrophobic core of HP35 were exposed completely; in contrast, the three aromatic residues in the hydrophobic core remained buried when binding the I-Gra surface. In addition, the two aromatic residues located at the helix-3 (Trp-23 and Phe-35) were involved in the interfacial binding on I-Gra.

4. Additional Simulation of HP35/D-Gra System with Duration of 1000 ns.

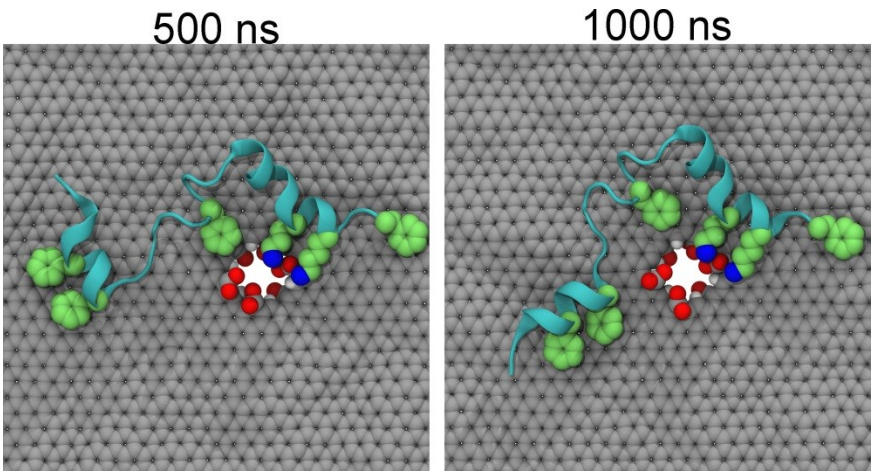

Figure S3. Snapshots of an additional simulation of HP35/D-Gra system at 500 ns and 1000 ns. The display setting is the same as Figure 1.

We also ran another simulation of the HP35/D-Gra system for a longer timescale (e.g. 1000 ns) to detect any structural change of HP35 on D-Gra after 500 ns (**Fig. S3**). Notably, at t = 500 ns, HP35 experienced serious structural deformation, losing most of its secondary structure which resembled the other three simulations (**Fig. 1B-D**). When t = 1000 ns, the secondary structure of HP35 showed no apparent change and the binding conformation showed limited fluctuation as compared to 500 ns.

5. Effect of ionic concentration and valence state to HP35 unfolding.

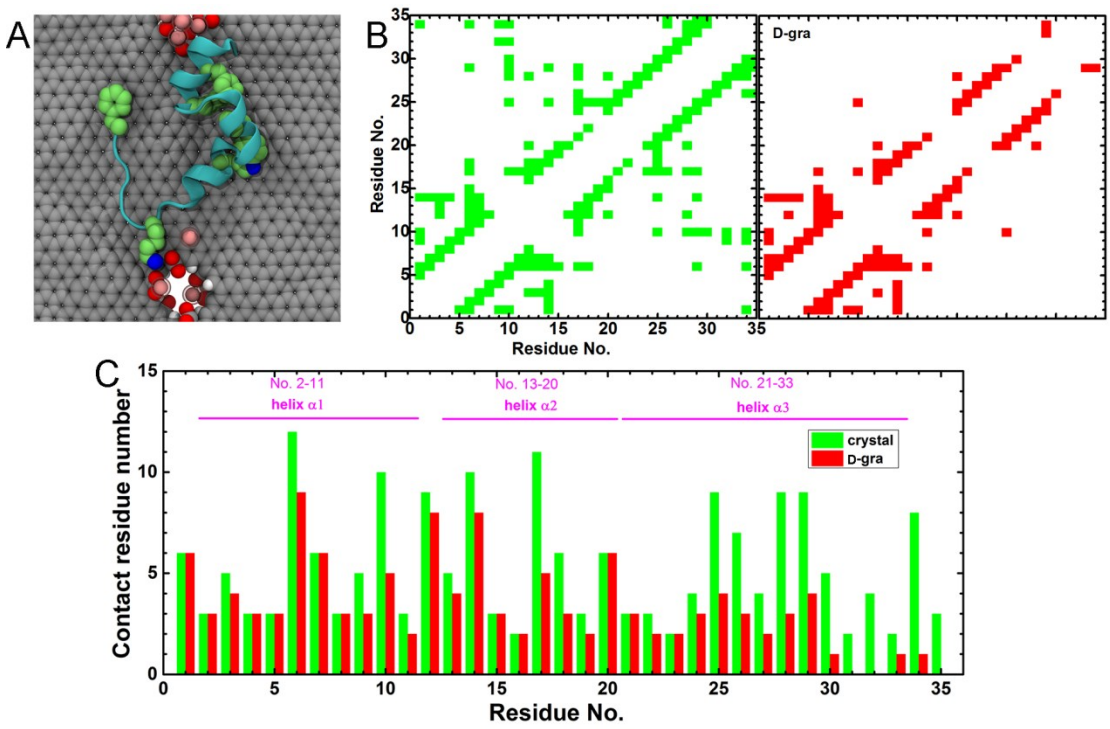

Figure S4. HP35 binding on D-Gra in 0.15 M NaCl solution. (A) The final conformation of HP35 binding on D-Gra in 0.15 M NaCl solution. The display setting is the same as Figure 1. The Na^+ ions adsorbed around the defect are shown with pink spheres. (B) The contact maps between all residues of HP35 in the first frame, i.e. the crystal structure (left), and in the last frame of HP35/D-Gra (right) simulation in 0.15 M NaCl solution. (C) The total number of native contacts that each residue formed in the first frame (green) and the last frame of HP35/D-Gra (red) simulation in 0.15 M NaCl solution.

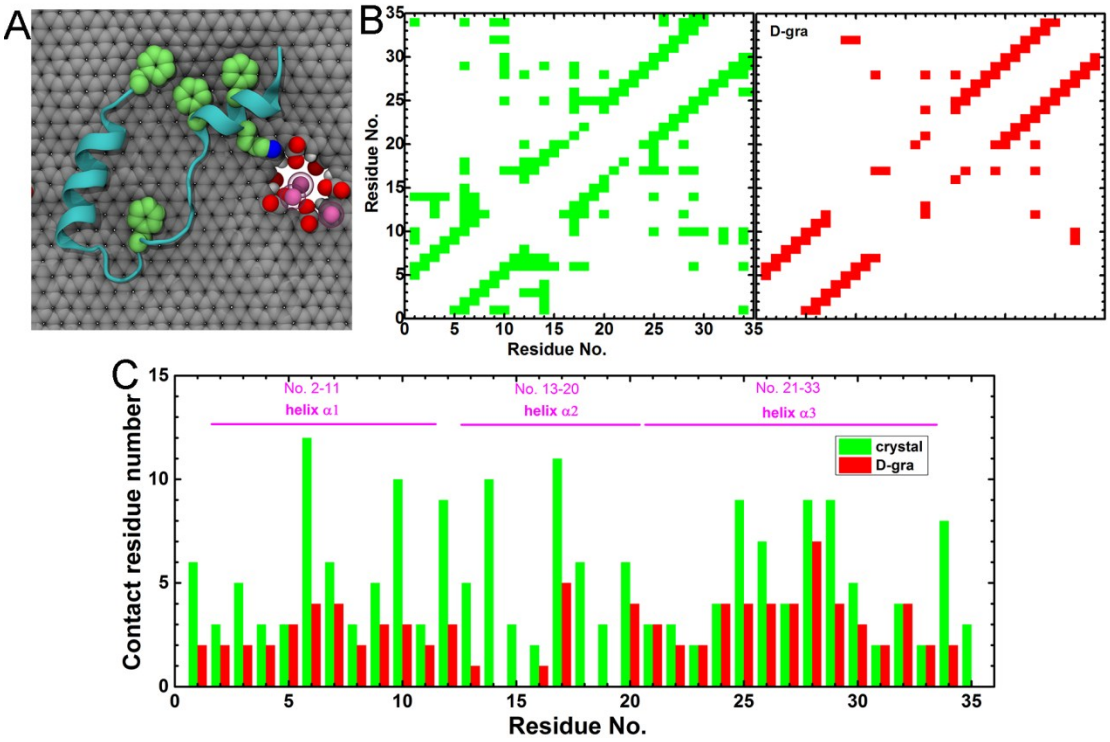

Figure S5. HP35 binding on D-Gra in 0.15 M $MgCl_2$ solution. (A) The final conformation of HP35 binding on D-Gra in 0.15 M $MgCl_2$ solution. The display setting is the same as Figure 1. The Mg^{2+} ions adsorbed around the defect are shown with mauve spheres. (B) The contact maps between all residues of HP35 in the first frame, i.e. the crystal structure (left), and in the last frame of HP35/D-Gra (right) simulation in 0.15 M $MgCl_2$ solution. (C) The total number of native contacts that each residue formed in the first frame (green) and the last frame of HP35/D-Gra (red) simulation in 0.15 M $MgCl_2$ solution.

Fig. S4 and **Fig. S5** illustrate the unfolding of HP35 on D-Gra in 0.15 M NaCl and $MgCl_2$ solutions to understand the effect of ionic concentration and valence state on HP35 unfolding. In 0.15 M NaCl solution, the unfolding of HP35 was observed where helix-3 disappeared partially along with some aromatic residues packing on the defect-free region of D-Gra and a lysine (Lys-29) directly contacting a defect. Similarly, HP35 also unfolded in 0.15 M $MgCl_2$ solution. Moreover, some cations were found near the defects which may generate local electrostatic screening for the attraction between the basic residues and the carboxyl groups of the defects and subsequently reduced the unfolding degree of HP35. In the $MgCl_2$ solution, the main change of HP35 was on helix-2, in which the native contacts were lost almost completely.

6. Defect-Assisted YAP65 Unfolding

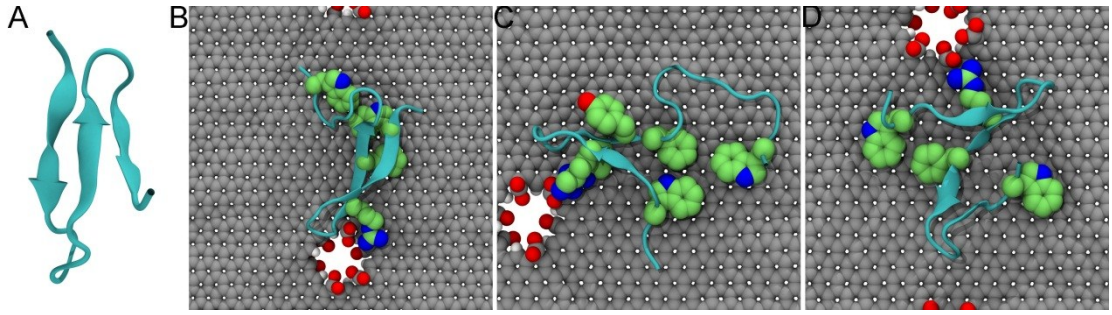

Figure S6. The YAP65 unfolding on the D-Gra. (A) The YAP65 protein secondary structure. (B-D) Last snapshots of YAP65 on D-Gra from three independent trajectories at 500 ns (only part of the graphene and defects near YAP65 are shown, with the sidechains of the key residues forming direct contacts with D-Gra highlighted).

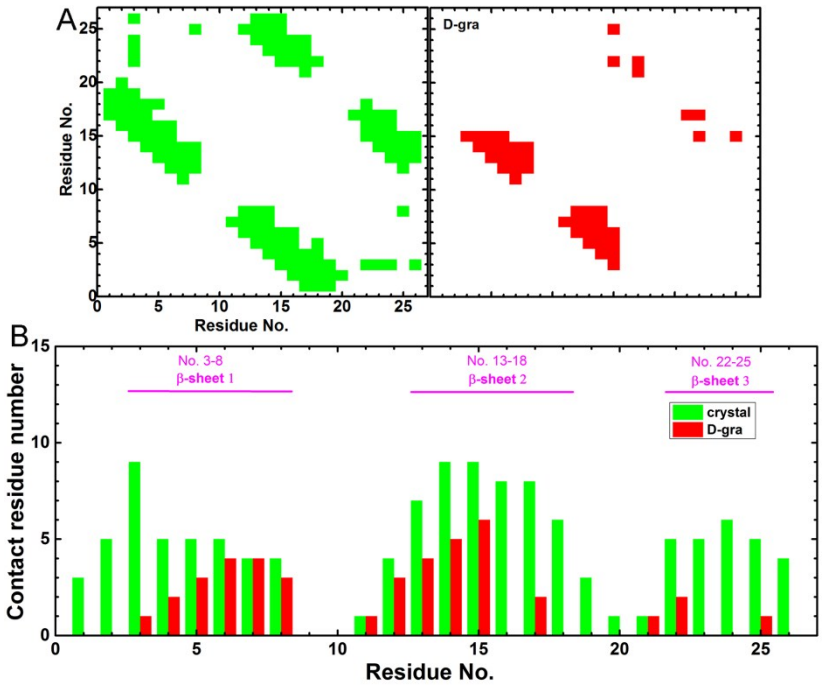

Figure S7. Structural analysis of YAP65 binding on D-Gra in a representative trajectory. (A) The contact maps between all residues of YAP65 in the first frame, i.e. the crystal structure (left), and in the last frame of YAP65/D-Gra (right) simulation. (B) The total number of native contacts that each residue formed in the first frame (green) and the last frame of YAP65/D-Gra (red) simulation.

The YAP65 protein is composed of three β-sheet segments (**Fig. S6A**), which is also a common protein model consisting of pure β-sheet structure used to explore the bio-nano interfacial binding.[28-29] For the system of YAP65 with D-Gra (**Fig. S6B-D**), denaturation was observed as YAP65 lost its structural integrity after 500 ns in all three trajectories. The sidechains of key residues that formed direct contacts with D-Gra were highlighted in these figures. Some aromatic residues (Trp-17, Tyr-28, Phe-29 and Trp-39) adsorbed to the defect-free regions of D-Gra through the formation of π-π stacking with the sp^2-hybridized carbon atoms, while some charged residues (Lys-21 and Arg-27) bound the defects. We further performed structural analysis of YAP65 binding on D-Gra using one of the trajectories (as shown in **Fig. S6C**) and summarized the results in **Fig. S7**. We found that the native contacts in half of β-sheet 2 and entire β-sheet 3 were lost almost completely and those in β-sheet 1 and the other half of β-sheet 2 were lost partially, which corresponded to the final conformation shown in **Fig. S6C**.

7. HP35 Structural Analysis from Parallel Trajectories

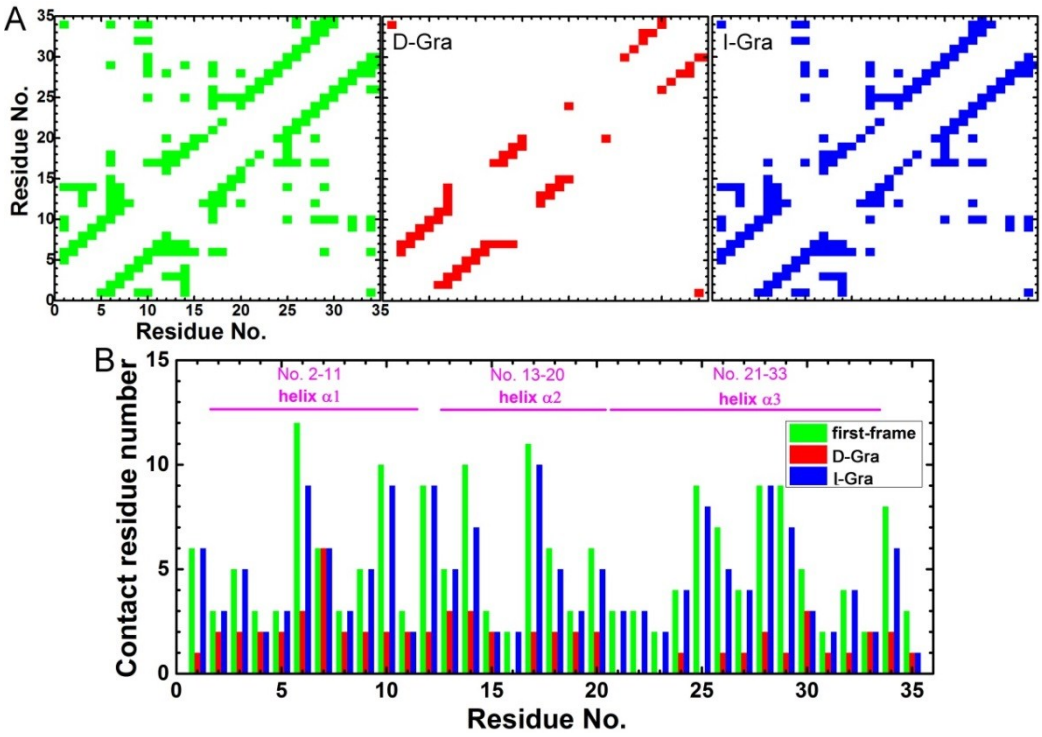

Figure S8 Results of the parallel trajectory #2. (A) The contact maps between the heavy atoms of HP35 in the first frame, i.e. the crystal structure (left), and in the last frames of HP35/D-Gra (middle) and HP35/I-Gra (right) simulations. (B) The total number of native contacts that each amino acid of HP35 formed in the first frame (green) and the last frames of HP35/D-Gra (red) and

HP35/I-Gra (blue) simulations.

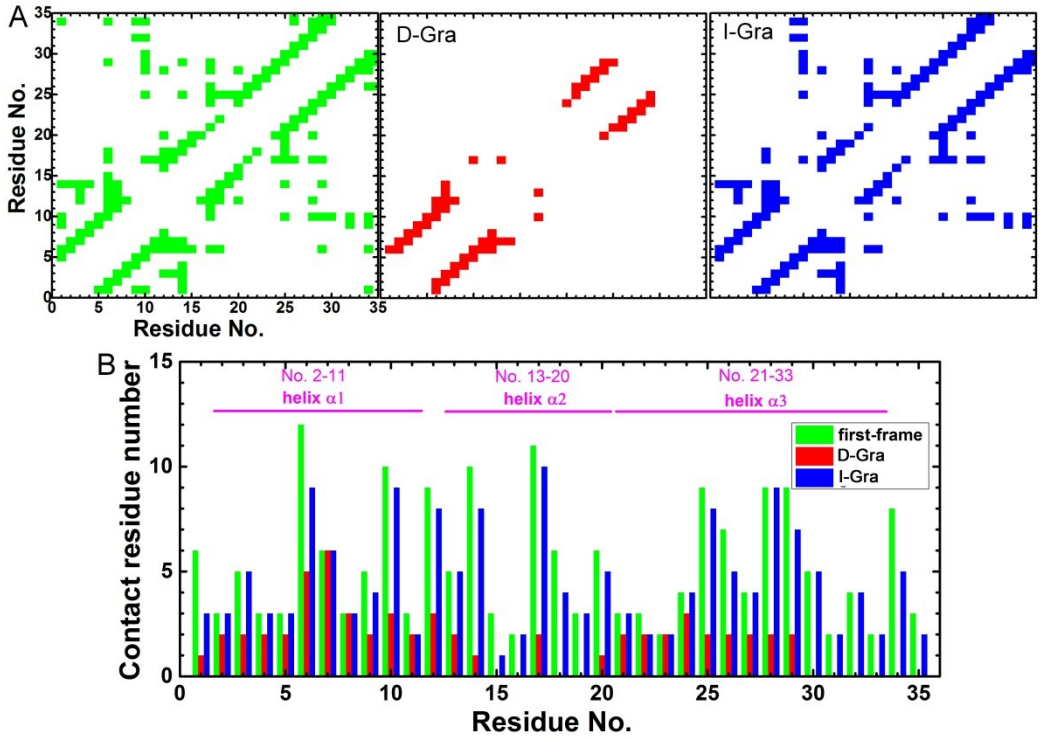

Figure S9. Results of the parallel trajectory #3. (A) The contact maps between the heavy atoms of HP35 in the first frame, i.e. the crystal structure (left), and in the last frames of HP35/D-Gra (middle) and HP35/I-Gra (right) simulations. (B) The total number of native contacts that each amino acid of HP35 formed in the first frame (green) and the last frames of HP35/D-Gra (red) and HP35/I-Gra (blue) simulations.

Fig. S8 and S9 depict the contact maps of HP35 in the crystal structure and the last frames of HP35/D-Gra and HP35/I-Gra in the parallel trajectories. In consistent with the results in Fig. 3 in the main manuscript, helix-2 and helix-3 of HP35 unfolded upon binding to D-Gra. The number of native contacts that each residue formed in the last frames of HP35/D-Gra trajectories also revealed a clear decrease as compared with that in the crystal structure. These results validate the stronger denaturing strength of D-Gra than that of I-Gra.

8. Transitory movements of Arg-14 show sharp increases of Coulombic energy.

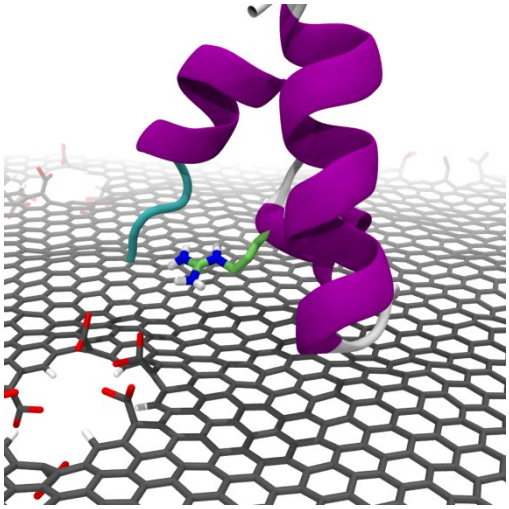

Figure S10. Snapshot of HP35 on D-Gra at 9.0 ns. Arg-14 moves away from the defect and results in sharp increases of Coulombic energy at 9.0 ns, which corresponds to Figure 4.

It is noted that at 9.0 ns, the Coulombic energy showed a transitory sharp increase to ~0 kcal/mol, indicating that the interaction between Arg-14 and the carboxyl groups of the defect disappeared for a short time, as shown in **Fig. S10**, where Arg-14 moved away from the defect.

9. Total interaction energies of HP35 denaturation upon binding to D-Gra

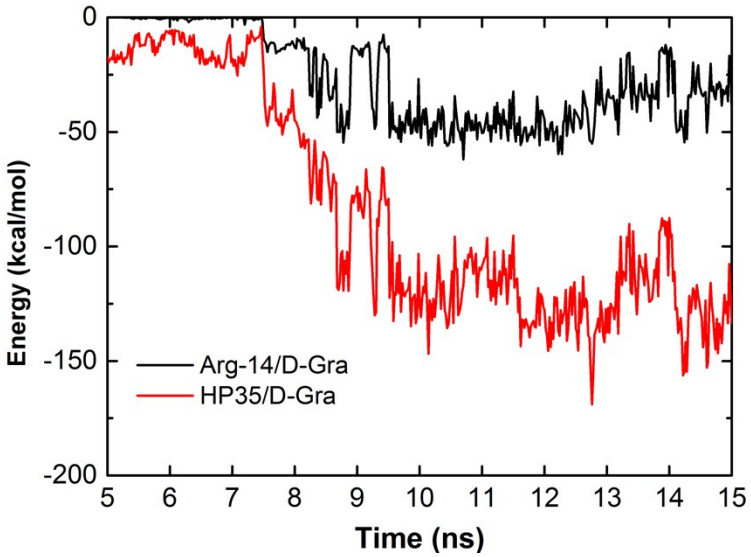

Figure S11. The total interaction energies (the sum of vdW and Coulomb energies) between Arg-14 and D-Gra (black) or between HP35 and D-Gra (red). The trajectory used in this analysis is the same

as that in **Fig. 4C**.

10. Mechanism Study of Defect-Assisted HP35 Unfolding

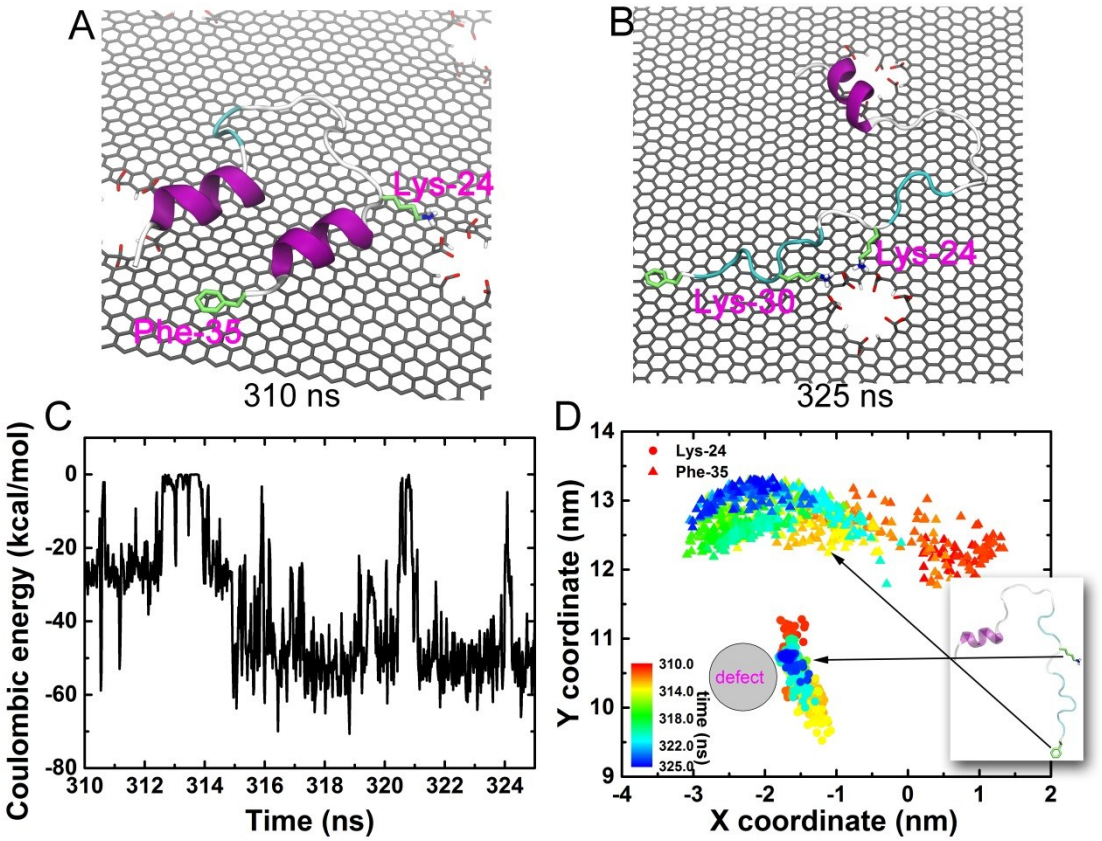

Figure S12. The unfolding process of helix-3 from 310 ns to 325 ns in the simulation. (A-B) Snapshots of HP35 on D-Gra at 310 ns and 325 ns, respectively. Three key residues (Phe-35, Lys-24, and Lys-30) that played important roles in the unfolding process are highlighted. (C) The coulombic energy between Lys-24 and the defect of D-Gra. (D) The trajectories of Phe-35 (triangles) and Lys-24 (circles) projected on the surface of D-Gra. The colors represent the time from 310 ns to 325 ns. Gray circle indicates the position of the defect.

In addition to the unfolding process of helix-2 discussed in the main manuscript, Fig. S12 depicts another unfolding process, the unfolding of helix-3, which completed in 15 ns. Fig. S12A depicts one snapshot at 310 ns, where helix-3 was still well maintained. The sidechain of Lys-24 formed electrostatic interaction with the carboxyl oxygen atoms of the defect, and thus the residue was restrained as the "anchor". The sidechain of Phe-35 formed π-π stacking with the C atoms at the defect-free regions of D-Gra. By 325 ns, helix-3 had totally unfolded, accompanied by the appearance of a second "anchor residue", Lys-30, at the defect site. During this process, Lys-24 had

always been attracted by the defect. The binding was strong which reached -50 kcal/mol (Fig. S12C). Through assessing the positions of Lys-24 and Phe-35, we concluded a similar mechanism of denaturation for helix-3, which was caused by the mobility-mismatch of "anchor residue" with the rest of the protein.

11. The function of water molecule in the initial adsorption as well as during residue's anchoring process.

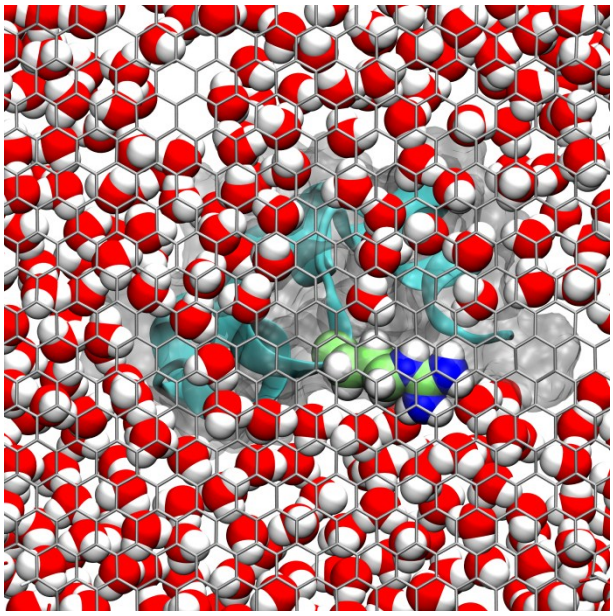

Figure S13. Interfacial waters between HP35 and D-Gra in the initial adsorption. The interfacial waters are shown with red (oxygen) and white (hydrogen) spheres, respectively. The HP35 is displayed by cyan ribbon and gray surface. The key residue, Arg-14, is shown with lime (carbon), blue (nitrogen) and white (hydrogen) spheres. The D-Gra is depicted with sticks.

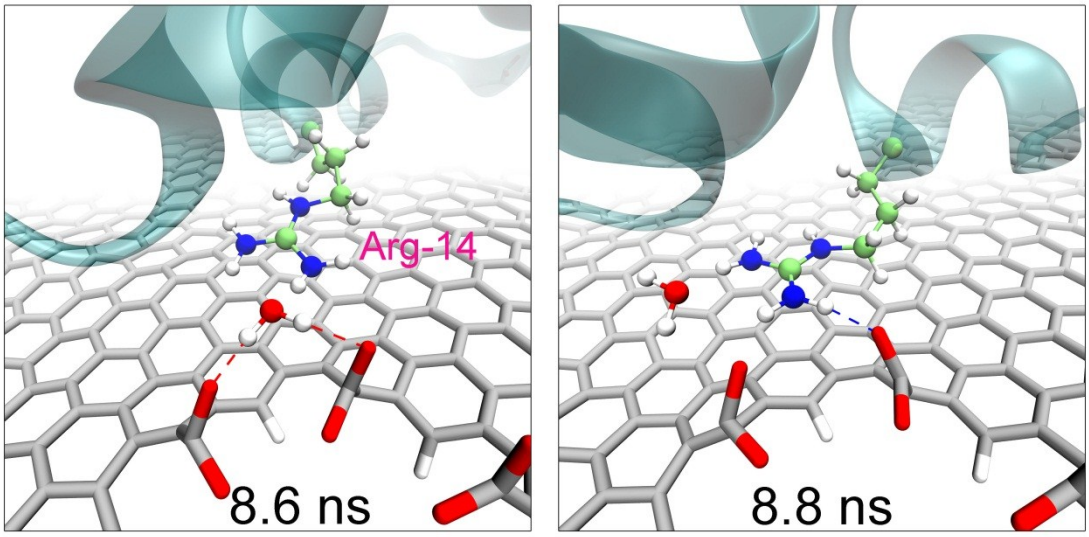

Figure S14. The key role of water molecule during Arg-14 anchoring process. The Arg-14 is shown by ball-and-stick model with carbon colored in lime, nitrogen colored in blue and hydrogen colored in white, respectively. The D-Gra is plotted by sticks. The water is displayed by ball-and-stick model colored in red and white. The red and blue dashed lines represent hydrogen bonds.

11. The stability of helix−1 when binding to D-Gra.

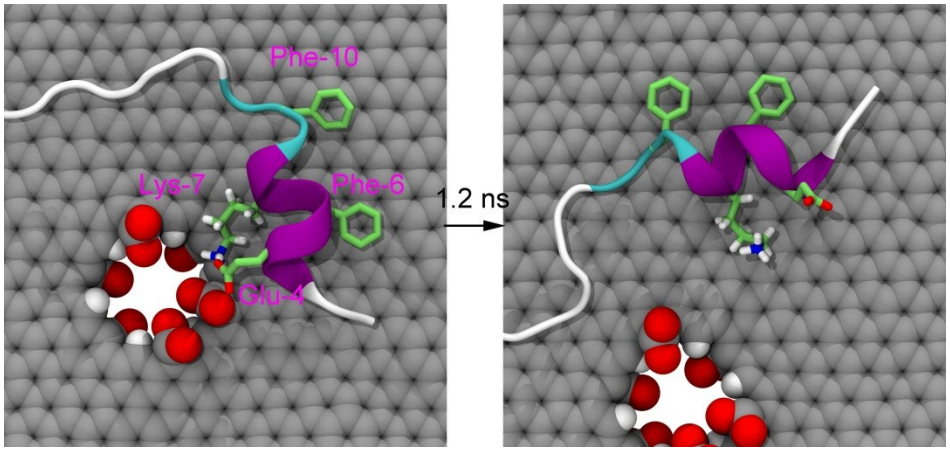

Figure S15. Binding conformation of helix-1 on D-Gra revealing the structural stability of helix-1. Four key residues (i.e., Glu-4, Phe-6, Lys-7 and Phe-10) that played important roles in the structural stability of helix-1 are labeled.

Reference

1. Snow, C. D.; Nguyen, N.; Pande, V. S.; Gruebele, M., Absolute comparison of simulated and

experimental protein-folding dynamics. *Nature* **2002,** *420* (6911), 102-106.

2. Shaw, D. E.; Maragakis, P.; Lindorff-Larsen, K.; Piana, S.; Dror, R. O., et al., Atomic-level characterization of the structural dynamics of proteins. *Science* **2010,** *330* (6002), 341-346.

3. Lei, H.; Wu, C.; Liu, H.; Duan, Y., Folding free-energy landscape of villin headpiece subdomain from molecular dynamics simulations. *P. Natl. Acad. Sci. USA* **2007,** *104* (12), 4925-4930.

4. Duan, Y.; Kollman, P. A., Pathways to a protein folding intermediate observed in a 1-microsecond simulation in aqueous solution. *Science* **1998,** *282* (5389), 740-744.

5. Chiu, T. K.; Kubelka, J.; Herbst-Irmer, R.; Eaton, W. A.; Hofrichter, J., et al., High-resolution x-ray crystal structures of the villin headpiece subdomain, an ultrafast folding protein. *P. Natl Acad. Sci. USA* **2005,** *102* (21), 7517-7522.

6. Pires, J. R.; Taha-Nejad, F.; Toepert, F.; Ast, T.; Hoffmuller, U., et al., Solution structures of the yap65 ww domain and the variant l30 k in complex with the peptides gtppppytvg, n-(n-octyl)-gpppy and plppy and the application of peptide libraries reveal a minimal binding epitope. *J. Mol. Biol.* **2001,** *314* (5), 1147-1156.

7. Hess, B.; Kutzner, C.; van der Spoel, D.; Lindahl, E., Gromacs 4: Algorithms for highly efficient, load-balanced, and scalable molecular simulation. *J. Chem. Theory Comput.* **2008,** *4* (3), 435-447.

8. Mackerell, A. D.; Feig, M.; Brooks, C. L., Extending the treatment of backbone energetics in protein force fields: Limitations of gas-phase quantum mechanics in reproducing protein conformational distributions in molecular dynamics simulations. *J. Comput. Chem.* **2004,** *25* (11), 1400-1415.

9. MacKerell, A. D.; Bashford, D.; Bellott, M.; Dunbrack, R. L.; Evanseck, J. D., et al., All-atom empirical potential for molecular modeling and dynamics studies of proteins. *J. Phys. Chem. B* **1998,** *102* (18), 3586-3616.

10. Bellido, E. P.; Seminario, J. M., Molecular dynamics simulations of folding of supported graphene. *J. Phys. Chem. C* **2010,** *114* (51), 22472-22477.

11. Jorgensen, W. L.; Chandrasekhar, J.; Madura, J. D.; Impey, R. W.; Klein, M. L., Comparison of simple potential functions for simulating liquid water. *J. Chem. Phys.* **1983,** *79* (2), 926-935.

12. Bussi, G.; Donadio, D.; Parrinello, M., Canonical sampling through velocity rescaling. *J. Chem. Phys.* **2007,** *126* (1), 014101.

13. Parrinello, M.; Rahman, A., Polymorphic transitions in single-crystals - a new molecular-dynamics method. *J. Appl. Phys.* **1981,** *52* (12), 7182-7190.

14. Zhu, W. J.; Low, T.; Perebeinos, V.; Bol, A. A.; Zhu, Y., et al., Structure and electronic transport in graphene wrinkles. *Nano Lett.* **2012,** *12* (7), 3431-3436.

15. Katoch, J.; Kim, S. N.; Kuang, Z. F.; Farmer, B. L.; Nalk, R. R., et al., Structure of a peptide adsorbed on graphene and graphite. *Nano Lett.* **2012,** *12* (5), 2342-2346.

16. Zhang, L. M.; Wang, Z. L.; Lu, Z. X.; Shen, H.; Huang, J., et al., Pegylated reduced graphene oxide as a superior ssrna delivery system. *J. Mater. Chem. B* **2013,** *1* (6), 749-755.

17. Hughes, Z. E.; Walsh, T. R., What makes a good graphene-binding peptide? Adsorption of amino acids and peptides at aqueous graphene interfaces. *J. Mater. Chem. B* **2015,** *3* (16), 3211-3221.

18. Hughes, Z. E.; Tomasio, S. M.; Walsh, T. R., Efficient simulations of the aqueous bio-interface of graphitic nanostructures with a polarisable model. *Nanoscale* **2014,** *6* (10), 5438-5448.

19. Dragneva, N.; Floriano, W. B.; Stauffer, D.; Mawhinney, R. C.; Fanchini, G., et al., Favorable adsorption of capped amino acids on graphene substrate driven by desolvation effect. *J. Chem. Phys.* **2013,** *139* (17), 174711.

20. Zou, X. Q.; Wei, S.; Jasensky, J.; Xiao, M. Y.; Wang, Q. M., et al., Molecular interactions between

graphene and biological molecules. *J. Am. Chem. Soc.* **2017,** *139* (5), 1928-1936.

21. Mukhopadhyay, T. K.; Bhattacharyya, K.; Datta, A., Gauging the nanotoxicity of h2d-c2n toward single-stranded DNA: An in silico molecular simulation approach. *Acs Appl Mater Inter* **2018,** *10* (16), 13805-13818.

22. Gu, Z.; Zhao, L.; Liu, S.; Duan, G.; Perez-Aguilar, J. M., et al., Orientational binding of DNA guided by the c2n template. *ACS Nano* **2017,** *11* (3), 3198-3206.

23. Essmann, U.; Perera, L.; Berkowitz, M. L.; Darden, T.; Lee, H., et al., A smooth particle mesh ewald method. *J. Chem. Phys.* **1995,** *103* (19), 8577-8593.

24. Darden, T.; York, D.; Pedersen, L., Particle mesh ewald - an n.Log(n) method for ewald sums in large systems. *J. Chem. Phys.* **1993,** *98* (12), 10089-10092.

25. Hess, B.; Bekker, H.; Berendsen, H. J. C.; Fraaije, J., Lincs: A linear constraint solver for molecular simulations. *J. Comput. Chem.* **1997,** *18* (12), 1463-1472.

26. Miyamoto, S.; Kollman, P. A., Settle - an analytical version of the shake and rattle algorithm for rigid water models. *J. Comput. Chem.* **1992,** *13* (8), 952-962.

27. Humphrey, W.; Dalke, A.; Schulten, K., Vmd: Visual molecular dynamics. *J. Mol. Graph. Model.* **1996,** *14* (1), 33-38.

28. Ling, Y.; Gu, Z.; Kang, S.-g.; Luo, J.; Zhou, R., Structural damage of a beta-sheet protein upon adsorption onto molybdenum disulfide nanotubes. *J. Phys. Chem. C* **2016,** *120* (12), 6796-6803.

29. Gu, Z.; De Luna, P.; Yang, Z.; Zhou, R., Structural influence of proteins upon adsorption to mos2 nanomaterials: Comparison of mos2 force field parameters. *Phys. Chem. Chem. Phys.* **2017,** *19* (4), 3039-3045.